Innovative coatings for reducing flow-induced cylinder noise by altering the sound diffraction

Zamponi, R.; Ragni, D.; van der Zwaag, S.; Avallone, F.

Important note
To cite this publication, please use the final published version (if applicable).
Please check the document version above.

Innovative coatings for reducing flow-induced cylinder noise by altering the sound diffraction ⓕ

R. Zamponi ✉ ⓘ ; D. Ragni ⓘ ; S. van der Zwaag ⓘ ; F. Avallone ⓘ

Check for updates

View Online   Export Citation   CrossMark

Innovative coatings for reducing flow-induced cylinder noise by altering the sound diffraction ⓕ

View Online   Export Citation   CrossMark

R. Zamponi,[1,a)] ⓘ D. Ragni,[1] ⓘ S. van der Zwaag,[2] ⓘ and F. Avallone[3] ⓘ

AFFILIATIONS

[1]Department of Flow Physics and Technology, Delft University of Technology, 2629HS Delft, Kluyverweg 1, The Netherlands
[2]Department of Aerospace Structures and Materials, Delft University of Technology, 2629HS Delft, Kluyverweg 1, The Netherlands
[3]Dipartimento di Ingegneria Meccanica e Aerospaziale, Politecnico di Torino, Corso Duca degli Abruzzi 24, 10129 Torino, Italy

[a)]Author to whom correspondence should be addressed: r.zamponi@tudelft.nl. Also at von Karman Institute for Fluid Dynamics, Waterloosesteenweg 72, B-1640 Sint-Genesius-Rode, Belgium

ABSTRACT

The aerodynamic noise radiated by the flow past a cylinder in the subcritical regime can be modeled by a quadrupolar sound source placed at the onset position of the vortex-shedding instability that is scattered by the surface with a dipolar directivity. When the cylinder is coated with a porous material, the intensity of the shed vortices is greatly reduced, determining a downstream shift of the instability-outbreak location. Consequently, sound diffraction is less efficient, and noise is mitigated. In this paper, an innovative design approach for a flow-permeable coating based on a further enhancement of such an effect is proposed. The results of phased-microphone-array measurements show that, once the leeward part of the cover is integrated with components that make the flow within the porous medium more streamlined, the quadrupolar source associated with the vortex-shedding onset is displaced more downstream, yielding additional noise attenuation of up to 10 dB with respect to a uniform coating. Furthermore, the same noise-control mechanism based on the weakening of the sound scattering can be exploited when these components are connected to the bare cylinder without the porous cover. In this case, the mitigation of overall sound pressure levels is comparable to that induced by the coated configurations due to the lack of noise increase produced by the inner flow interacting within the pores of the material. Remarkable sound reductions of up to 10 dB and a potential drag-force decrease are achieved with this approach, which paves the way for disruptive and more optimized noise-attenuation solutions.

I. INTRODUCTION

When a fluid flows past a circular cylinder, it induces a complex pattern of vortices and turbulent eddies that can result in significant aerodynamic sound. The noise produced by this phenomenon, which affects applications that range from landing-gear systems to high-speed trains, can be decomposed into a tonal and broadband component. The former, referred to as Aeolian tone, is characterized by a distinct frequency and is a consequence of the shedding of turbulent eddies that periodically detach from opposite sides of the cylinder.[1] Decreasing the unsteadiness of this repeating pattern, i.e., the so-called von Kármán street, has a beneficial effect on the emitted sound.[2]

One of the most promising passive flow-control strategies to reduce the Aeolian tone by controlling the vortex shedding is to coat the surface of the cylinder with a porous material. In the last few decades, numerous experimental and numerical studies have been conducted to evaluate the effectiveness of flow-permeable coatings in

decreasing noise. Sueki et al.[3] first demonstrated that this technological solution was able to mitigate aerodynamic sound by suppressing the unsteady motion of the turbulent structures that, in turn, decreases the pressure fluctuations on the surface. This stabilization effect of the oscillating wake was explained by Naito and Fukagata[4] in terms of slip velocity and fluid energy. Liu et al.[5] showed that incorporating a flow-permeable cover could lower the frequency at which vortex-shedding occurs and narrow its frequency range, reducing, in turn, the radiated noise. This effect becomes more significant with greater thickness, porosity, and average pore size of the porous layer. Similar results were found for cylinders coated with metal foam by Aguiar et al.[6] Showkat Ali et al.[7] demonstrated that the most significant effect of the porous coating of the cylinder on the flow field is to displace the vortex-formation region downstream and reduce the turbulence kinetic energy in the near wake. Furthermore, the study of Geyer and Sarradj[8] indicated that porous materials with high air-flow permeability offer

the most effective noise mitigation. Comparable findings were obtained by Geyer,[9] who determined basic trends for the estimation of the most important parameters acting on the Strouhal number and energy content of the Aeolian tone, i.e., porous-layer thickness, porosity, and airflow resistivity, by means of the method of linear regression.

Moreover, novel solutions for the integration of porosity based on structured 3D-printed covers were recently proposed. Arcondoulis *et al.*[10] designed a structured porous coating whose porosity and permeability could be modified independently. They demonstrated that such a design could yield comparable vortex-shedding-tone suppression and frequency shift in the acoustic power spectral density to that obtained with randomized permeable foams with the same parameters. In addition to the possibility of investigating the flow field within the porous medium due to a more accessible optical access,[11] this structured coating offers the advantage of integrating nonuniform innovative solutions where the porosity varies along the span or circumference of the porous cover.[12,13] A similar design was also suggested by Bathla and Kennedy,[14] who evaluated the suitability of masked stereolithography (MSLA) 3D printers for manufacturing coatings based on unit cells made of self-supporting lattices. Notably, they showed that employing partial covers with a helicoidal or spaced shape results in comparable flow-stabilization performance to that of a full coating while considerably reducing the material consumption. Nevertheless, the sound-control capabilities of this technological solution have not been investigated yet.

In this study, a new design for a nonuniform coating of a cylinder based on the maximization of the vortex-formation length is presented. Such a strategy is supported by recent findings from the authors,[15] who demonstrated that the dominant noise sources produced by the flow past a circular cylinder in the beamforming sound maps are located in the wake of the body, specifically at the onset of the shedding instability. This region is associated with the origin of an equivalent quadrupolar source that radiates into the far field and is scattered by the body surface. The efficiency of such a diffraction mechanism is expected to decrease exponentially with the increasing distance from the body, as typically occurs for acoustically compact cases.[16] Therefore, optimizing the downstream shift of the vortex-shedding onset position represents a valid design criterion for the aeroacoustic treatment of the cylinder and has inspired the technological solutions developed in this research. To verify the effectiveness of the proposed approach, several coating prototypes built upon the modification of existing metal-foam covers have been manufactured and tested at the A-Tunnel facility of the Delft University of Technology (TU Delft) by means of phased-microphone-array measurements.

The remainder of the paper is structured as follows: The physical mechanism behind the Aeolian-tone generation and the noise-reduction mechanism associated with the porous coating of a circular cylinder are reviewed in Sec. II. The experimental setup built for the measurement campaign is illustrated in Sec. III. In Sec. IV, the main aeroacoustic outcomes are presented and discussed, highlighting the connection between the alteration and the sound scattered by the body and the noise mitigation provided by the proposed coatings. Finally, the concluding remarks are given in Sec. V.

II. THEORY

A. Formulation of cylinder flow-induced noise

The flow-induced cylinder noise at low Mach numbers can be formulated as a 2D diffraction problem where the sound emitted by equivalent quadrupolar volume sources in the flow are scattered by the cylinder surface.[16] This subsection provides a brief overview of the equations describing this phenomenon. The coordinate system defined for the formulation of the problem is depicted in Fig. 1.

The inhomogeneous Helmholtz equation expressed in the frequency domain for an observer located at $\boldsymbol{x}$ reads

$$(\nabla^2 + k_0^2)\,\hat{p}(\boldsymbol{x}, \omega) = \hat{q}(\boldsymbol{x}, \omega), \tag{1}$$

k_0 being the acoustic wavenumber ω/c_∞, where ω and c_∞ are the angular frequency and speed of sound, respectively, $\hat{p}$ being the unsteady-pressure field within the acoustic region, and $\hat{q}$ being the source field. $\hat{p}$ and $\hat{q}$ are mathematically defined in a finite volume V containing a surface S (see Fig. 1). Equation (1) can be solved using the convolution product with the frequency-domain Green's function that, for a point source in $\boldsymbol{y}$, satisfies

$$(\nabla^2 + k_0^2)\,\hat{G}(\boldsymbol{x}|\boldsymbol{y}, \omega) = \delta(\boldsymbol{x} - \boldsymbol{y}). \tag{2}$$

δ is here the Dirac function. Afterward, integrating by parts and applying Green's theorem result in

$$\hat{p}(\boldsymbol{x}, \omega) = \iiint_V \hat{q}(\boldsymbol{y}, \omega)\,\hat{G}(\boldsymbol{x}|\boldsymbol{y}, \omega)\,\mathrm{d}V$$
$$+ \iint_S \left[\hat{G}(\boldsymbol{x}|\boldsymbol{y}, \omega) \frac{\partial \hat{p}(\boldsymbol{y}, \omega)}{\partial y_i} - \hat{p}(\boldsymbol{y}, \omega) \frac{\partial \hat{G}(\boldsymbol{x}|\boldsymbol{y}, \omega)}{\partial y_i} \right] n_i\,\mathrm{d}S, \tag{3}$$

with $\boldsymbol{n}$ being the inward-pointing normal on S.

The source term $\hat{q}$ is computed by means of Lighthill's analogy[17]

$$\hat{q} = -\frac{\partial^2 \hat{T}_{ij}}{\partial x_i \partial x_j}, \tag{4}$$

where $\hat{T}_{ij}$ is the Fourier transform of Lighthill's stress tensor $T_{ij} = \rho u_i u_j - \sigma_{ij} + (p' - c_\infty^2 \rho')\,\delta_{ij}$ that models the sound generated by Reynolds stresses $\rho u_i u_j$, ρ and $\hat{u}_i$ being the density and flow velocity, respectively, viscous stresses σ_{ij}, and nonisentropic processes. The volume integral in Eq. (3) can then be reformulated, exploiting the integration by parts, which makes it possible to shift the partial
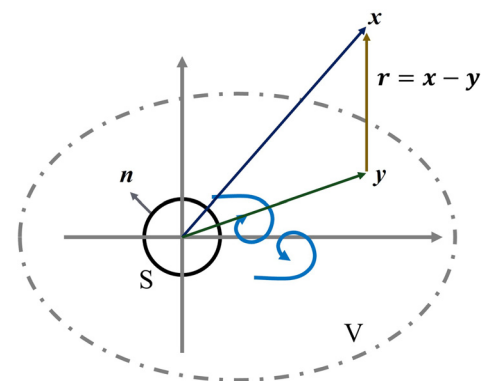

FIG. 1. Coordinate system defined for formulating the flow-induced cylinder noise as a diffraction problem. The cylinder has a diameter of d.

02 January 2024 12:36:44

derivatives from the source to $\hat{G}$, and using the divergence theorem and the symmetry property of $\hat{T}_{ij}$.

Owing to the assumed high Reynolds number, the viscous stresses are neglected with respect to the pressure fluctuations and Reynolds stresses in the surface integral. At the surface, which is considered nonvibrating and solid, $\hat{u}_i$ is null for the no-slip condition, while $\partial \hat{p}/\partial n = 0$ is zero due to the rigidity condition. As a consequence, Eq. (3) reads

$$\hat{p}(\boldsymbol{x}, \omega) = -\iiint_V \frac{\partial^2 \hat{G}}{\partial y_i \partial y_j} \, \hat{T}_{ij} \, \mathrm{d}V - \iint_S \hat{p} \, \frac{\partial \hat{G}}{\partial y_i} \, n_i \, \mathrm{d}S. \quad (5)$$

Any arbitrary $\hat{G}$ makes it possible to solve Eq. (5). If the free-field Green's function $\hat{G}_0$ is adopted, Eq. (5) takes the form of Curle's analogy[18]

$$\hat{p}(\boldsymbol{x}, \omega) = -\iiint_V \frac{\partial^2 \hat{G}_0}{\partial y_i \partial y_j} \, \hat{T}_{ij} \, \mathrm{d}V - \iint_S \hat{p} \, \frac{\partial \hat{G}_0}{\partial y_i} \, n_i \, \mathrm{d}S. \quad (6)$$

Nevertheless, a tailored Green's function $\hat{G}_1$ such that $\partial \hat{G}_1/\partial n = 0$ on S can also be employed to take into account the acoustic response of the body. By doing so, the surface integral vanishes, resulting in

$$\hat{p}(\boldsymbol{x}, \omega) = -\iiint_V \frac{\partial^2 \hat{G}_1}{\partial y_i \partial y_j} \, \hat{T}_{ij} \, \mathrm{d}V. \quad (7)$$

Hence, the problem reduces to finding an adequate expression for $\hat{G}_1$. One possibility is to add a solution of the homogeneous Helmholtz equation to the free-field Green's function: $\hat{G}_1 = \hat{G}_0 + \hat{G}_s$. The latter term allows the boundary condition on the body surface to be satisfied and is denoted as the scattered term.

The comparison between Eqs. (6) and (7) indicates that the surface integral in Curle's analogy is linked to the component of the aerodynamic noise generated by the volume term scattered by the body[16]

$$\iint_S \hat{p} \, \frac{\partial \hat{G}_0}{\partial y_i} \, n_i \, \mathrm{d}S = \iiint_V \frac{\partial^2 \hat{G}_s}{\partial y_i \partial y_j} \, \hat{T}_{ij} \, \mathrm{d}V. \quad (8)$$

The surface term is thus reinterpreted as a different equivalent sound source, which maintains a dipolar directivity pattern in the far field, as the spatial derivative in the integral suggests.

B. Noise-reduction mechanism of the porous coating

As mentioned in Sec. I, the modifications of the coating shapes based on the decrease in the sound-scattering efficiency have been inspired by the conclusions drawn in a recent study from the authors.[15] The findings of this research reveal that, at the vortex-shedding frequency, flow-induced cylinder noise is generated by a compact elementary quadrupole radiating from the shedding-instability onset location and scattering into the far field, with a dipolar directivity, as a consequence of its diffraction by the body. This sound-generation mechanism is supported by the analytical framework outlined in Sec. II A. The direct and scattered acoustic fields radiate simultaneously, and the distance between the volume source and the surface determines their relative contributions.

From a physical perspective, Howe[19] suggested that the principal event that leads to the quadrupole generation in Eq. (7) is the sudden acceleration of the vorticity at the outbreak position of the shedding instability. The shed turbulent structures grow in strength within the shear layer until they are released into the flow and rapidly accelerate to the convection velocity at the end of the vortex-formation region. The deformation and acceleration of the vorticity field occur at the vortex-shedding frequency and may be associated with the interactions of two counter-rotating eddies as they encounter together after the vortex-formation length.[16]

When the porous coating is integrated, the unsteadiness of the vortical motion is greatly reduced, and the time variation of the vortex dynamics described above is weaker, attenuating the strength of the quadrupole. Indeed, under the assumptions of acoustic compactness and geometric far field, the volume sources of Lighthill's analogy in the time domain are dictated by the integral of the second derivative of T_{ij} with respect to time.[20] Furthermore, the increase in vortex-formation length has the striking result of moving the origin of this compact source downstream, decreasing, in turn, the efficiency of the sound scattering by acting on $\hat{G}_s$ [see Eq. (8)]. This effect has been demonstrated to make the most impactful contribution to noise mitigation. Hence, modifying the topology of the flow within the porous cover to enhance the vortex-formation length has the potential to further improve the sound-control capabilities of this technology. The idea behind the design principle that will be proposed in Sec. III C is to provide a more streamlined shape for the internal fluid within the permeable medium to follow. The ejection of less disturbed flow from the leeward part of the body can move the vortex-shedding outbreak position more downstream and, in turn, further decrease the efficiency of the sound diffraction by the surface.

III. METHODOLOGY

A. Wind-tunnel facility and cylinder specimen

The A-tunnel facility of the TU Delft is a vertical open-jet wind tunnel placed in an anechoic chamber equipped with Flamex Basic acoustic absorbing foam that results in a cutoff frequency of 250 Hz.[21] The outlet nozzle of the vertical tunnel is installed at the exit of the contraction, has a height of 1 m, and features a rectangular exit plane having a contraction ratio of 42 to 1, a span of $s = 0.250$ m, and a width of $w = 0.400$ m. The circular cylinder specimens are supported by two side plates, which guide the flow from the outlet nozzle and have a length equal to s. A schematic of the experimental arrangement is illustrated in Fig. 2, where the reference system used to present the results is reported. Specifically, the x-axis is aligned with the streamwise direction, the z-axis is aligned with the span of the specimen, and the y-axis is oriented in order to form a right-handed coordinate system. The origin is placed at the midspan of the trailing edge of the cylinder.

Several configurations have been tested: a bare cylinder, or baseline, a cylinder coated with a porous material, and different nonuniform covers designed as modifications of the coated configuration. As indicated in Zamponi et al.,[22] the diameter d of the inner specimen has been maintained constant to model the integration of external material into an existing device. The outer diameter D of the covered specimen is hence given by the coating thickness t, according to $D = d + 2t$. The geometry of the tested configurations allows the vortex-shedding instability to develop undisturbed,[23] minimizes the blockage exerted
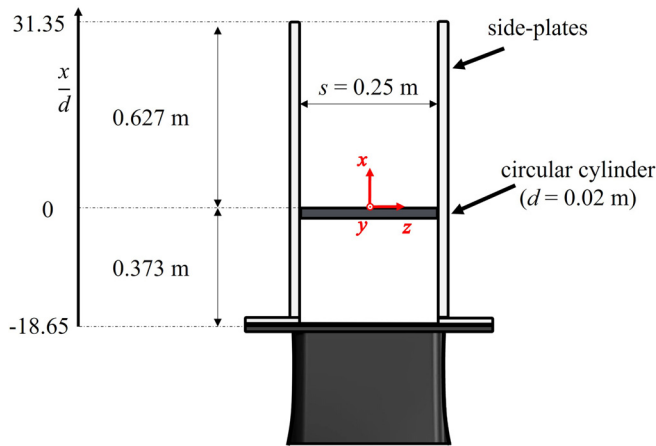
FIG. 2. Test section showing the outlet nozzle, side plates, and cylinder specimen, including the reference system considered for presenting the results.

by the body, and produces an Aeolian tone above the cutoff frequency of the anechoic facility. Moreover, the thickness of the cover should be large enough to permit the installation of the porous coating while maintaining its structural integrity. The resulting dimensions have been $d = 20$, $D = 30$, and $t = 5$ mm, leading to aspect ratios of $L/d = 12.5$ and $L/D = 8.33$.

The measurements have been carried out at free-stream flow velocities in the subcritical regime ranging from $U_\infty = 25$ to $U_\infty = 50$ ms^{-1} that result in Reynolds numbers based on the inner cylinder diameter of $Re_d = 3.4 \times 10^4$ and $Re_d = 6.8 \times 10^4$, respectively. The flow speed is measured through a Pitot static tube plugged into a Mensor DPG 2400 pressure gauge and having an accuracy of 0.03% of the read value. From previous analyses, the mean velocity in the streamwise direction was found to be uniform within 0.6% independently of the free-stream velocity, whereas the turbulence intensity of the clean flow was below 0.1% for the entire range of operative velocities.[21]

B. Porous coating

The porous coating is made of a nickel Ni open-cell metal foam manufactured through the electrodeposition of pure nickel on a polyurethane foam, which results in a homogeneous microstructure based on a dodecahedron-shaped cell. This material has already been used for analogous measurement campaigns by several authors.[3,6,10] The metal foam possesses a nominal cell diameter of 10 PPI, the PPI being a non-SI unit usually employed as an indication of the number of pores per inch, and a porosity φ, which is defined as the ratio of the void volume to the total volume, of 95%. These values are similar to those considered in the literature results mentioned in Sec. I.

The characterization of the porous media has been performed using the experimental rig described by Rubio Carpio et al.[24] This technique consists of least squares fitting the Hazen–Dupuit–Darcy quadratic equation[25]

$$\frac{\Delta p}{t_s} = \frac{\mu}{K} v_d + \rho C v_d^2, \tag{9}$$

Δp being the pressure drop across a homogeneous porous material sample with thickness t_s, μ the fluid dynamic viscosity, v_d the Darcian

velocity, which is determined as the ratio of the volumetric flow rate to the cross-section area of the material sample, and K and C the static permeability and form coefficient of the porous medium, which account for pressure losses due to viscous and inertial effects, respectively. In addition, the term $R = \Delta p/(t_s v_d)$ denotes the static air-flow resistivity of the material. An ensemble of 20 values of pressure drop, corresponding to Darcian velocities ranging between 0 and 2.5 ms^{-1}, are considered for fitting Eq. (9).

Two pressure ports are placed 50 mm upstream and downstream of the test section and are connected to a Mensor DPG 2101 pressure gauge featuring an accuracy of 2 Pa. The volumetric flow rate is controlled through an Aventics pressure regulator and evaluated by a TSI 4040 volumetric flow meter that is located upstream of the pipe and has an accuracy of 2% of the read value.

The porous-material samples are 55 mm metal-foam disks inserted in a hollow aluminum cylinder, which is placed in the test section. A parametric study on t_s has been carried out to prevent the occurrence of entrance or exit effects on the measured pressure drop, which may prevail if the thickness of the sample is smaller or comparable to the pore diameter.[26,27] Hence, t_s has been varied between 40 and 120 mm. The convergence in the values of K and C has been found for the thickest samples, hinting that spurious effects, in that case, could be assumed negligible. The outcome of the characterization is reported in Table I and shows that the metal foam designed in this research features low static air-flow resistivity if compared to the range of porous materials typically employed in wind tunnel tests. According to Sharma et al.,[28] a small value of R is essential in achieving noise reduction from a porous-covered cylinder, and this parameter should be carefully tuned together with the coating thickness to control the aeroacoustic performance of this technological solution.

Finally, a thorough analysis of the flow-field alterations induced by this cover with respect to a bare cylinder in the subcritical regime is reported by Zamponi et al.,[15] who observed that the main effect of the metal-foam coating is to stabilize the cylinder wake, which leads to an elongation of the vortex-formation length and a decrease in the turbulence kinetic energy. These results are consistent with the literature findings reviewed in Sec. I.

C. Modifications of the porous coating

A graphical overview of all tested covers and the related nomenclature is given in Fig. 3(a). Two different sleeves, denoted as *insert* and *tail*, have been designed to be rigidly connected to the leeward part of the bare-cylinder specimen. The former component is shaped as an annulus sector beveled in correspondence with the outer edges and projected onto the spanwise direction, the annulus being characterized by the same geometry as the porous coating. The latter component shares the basis of the insert, but, in this case, the sides of its section extend beyond the outer circumference arc until they intersect [see Fig. 3(a)].

TABLE I. Measured properties for the metal-foam samples. Quantities in parentheses refer to the nominal values provided by the manufacturer.

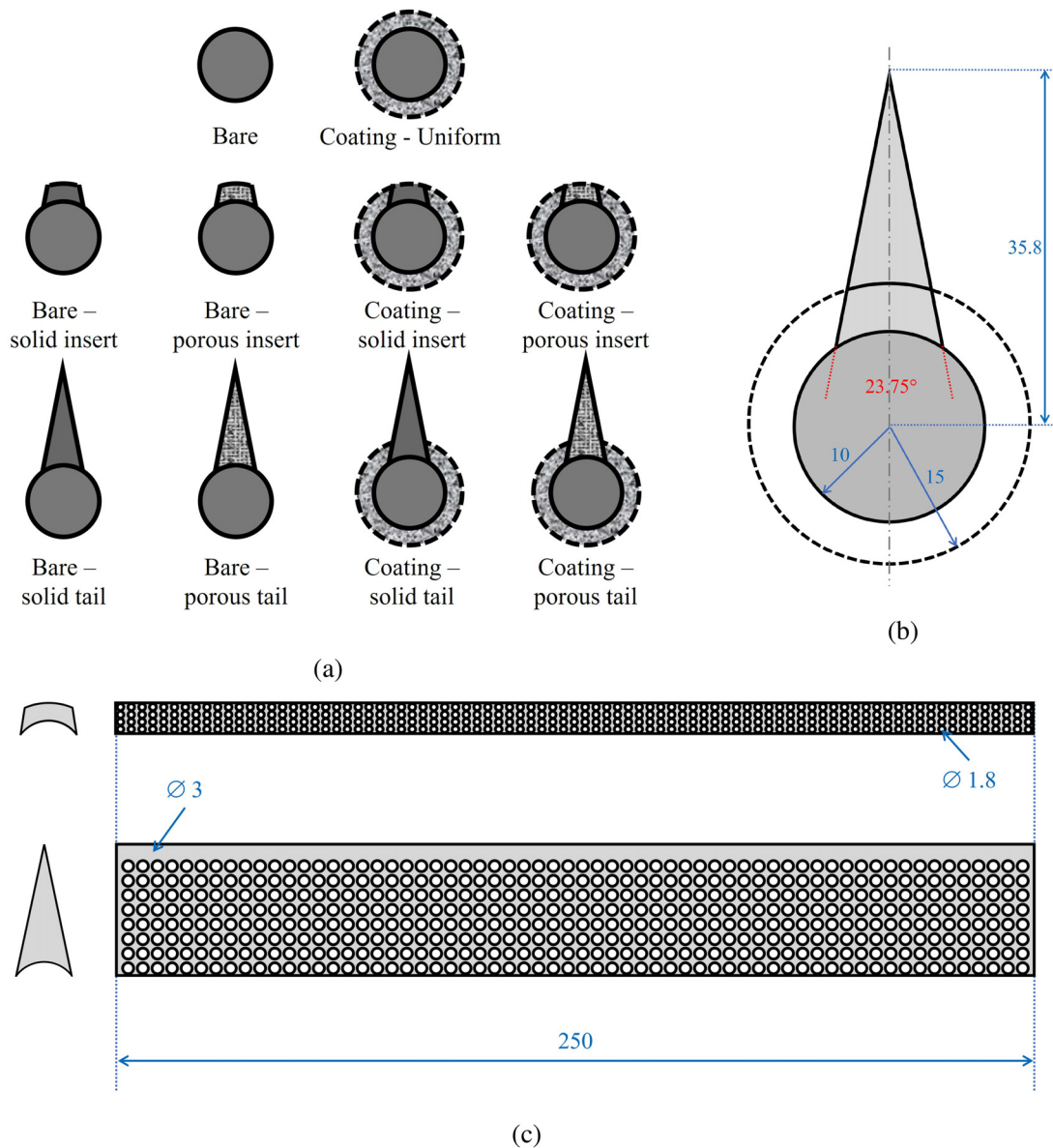| PPI	φ (%)	R (Nsm^{-4})	K (m^2)	C (m^{-1})
(10)	(95)	4.148×10^1	4.371×10^{-7}	1.103×10^2

FIG. 3. (a) Overview and nomenclature of the tested configurations based on the bare and coated cylinders. (b) Geometrical dimensions of the coating modifications. (c) Schematic of the porous insert and tail. Distances are given in mm.

Regarding the design of the sleeves, the insert has been dimensioned by analyzing the typical streamlines of the internal flow within the cover from the numerical investigations outlined in Sec. I. This is expected to shift the flow-recirculation region, and thereby the origin of the quadrupolar sources, more downstream, thanks to the higher energy level possessed by the fluid ejected in the leeward part of the body. In other words, the aim is to modify the topology of the flow within the material to enhance the noise-mitigation mechanism induced by the coating. One research question associated with the insert concerns its streamwise extension: is there a maximum optimal length that is capable of granting optimal sound reduction? Indeed, it is reasonable to expect that, above a certain length, the cylinder would

start acting as a thick, blunt airfoil. In this case, a different noise-production mechanism, possibly linked to the scattering of the turbulent boundary layer forming on this component, would be expected. The tail serves to verify such an assumption.

Furthermore, two configurations have been 3D printed using polyamide 12 for each sleeve: a solid, which is impermeable to flow, and a porous one, which features perforations oriented along the azimuthal direction with respect to the cylinder center. The diameters of the perforations are 1.8 and 3 mm for the insert and tail, respectively. No communication in the radial direction is allowed here. These dimensions have been chosen in order to maintain approximately the same weight between the perforated pieces and the amount of metal

foam that is removed from the coating. The geometrical characteristics of the manufactured configurations are illustrated in Fig. 3(b). A sector shaped as the negative of the insert has been cut from the metal-foam cover to accommodate the components into the coated cylinder. The resulting sleeve can then be slid along the surface to form a sort of non-uniform porous coating.

D. Far-field acoustic measurements

A microphone array having 64 G.R.A.S. 40 PH analog free-field microphones with integrated constant-current power amplifiers is used for the far-field acoustic measurements. Each microphone has a diameter of 0.007 m and a length of 0.059 m and features a flat frequency response within ± 1 dB from 50 Hz to 5 kHz and within ± 2 dB from 5 to 20 kHz. The sensors are connected to a data acquisition system comprising 4 NI PXIe-4499 Sound and Vibration Modules with a 24 bits resolution and a 204.8 kHz maximum sampling rate. The boards are controlled by a NI RMC-8354 computer via a NI PXIe-8370 board. All the transducers are calibrated in amplitude using a G.R.A.S. 42AG pistonphone, emitting a sinusoidal wave of 94 dB at 1 kHz.

The microphone array is characterized by an aperture of around 2 m and is placed in an optimized multiarm spiral configuration[29] that is oriented parallel to the $x - z$ plane. Concerning the reference system illustrated in Sec. III A, the central microphone is located at $(x, y, z) = (5\,d, 59.25\,d, -0.25\,d)$. A schematic of the position of the microphone array relative to the test section is depicted in Fig. 4. For each configuration, the data have been acquired at a sampling frequency of 102.4 kHz for 20 s. For the tests, five free-stream Reynolds numbers have been considered, namely, $Re_d = 3.4 \times 10^4, 4.1 \times 10^4, 4.8 \times 10^4, 5.4 \times 10^4, 6.8 \times 10^4$, corresponding to free-stream flow speeds U_∞ ranging from 25 to 50 ms^{-1}.

The power spectral densities of the acoustic signals, which will be presented in Secs. IV A and IV B at a reference distance of 1 m, have been calculated by means of the Welch method,[30] with blocks of 2^{13} samples, corresponding to 0.16 s, windowed through a Hanning weighting function that has 50% of data overlap, hence delivering a frequency resolution of 12.5 Hz. For these parameters, the associated random error, considering a 95% confidence interval, is estimated to be on the order of 0.8 dB.[31]

Furthermore, the data have been subsequently post-processed with an in-house generalized inverse beamforming (GIB) technique[32] validated through numerical and experimental benchmark datasets[33,34] to provide accurate visualization of the noise sources. This method allows the determination of the sound-source distributions by inverting a model that links the eigenmodes of the cross-spectral matrix of the recorded microphone signals to the amplitude distribution of a set of prescribed potential sources. Each eigenmode is associated with a coherent source distribution, and only the first 3 most energetic modes have been computed since they were deemed sufficient to reconstruct the acoustic field at the frequency ranges of interest. The inversion is performed by solving an underdetermined L_p-norm minimization problem by means of an iterated reweighted least squares algorithm, where p has been set to 0.9 to enforce the sparsity of the solution. Since the problem is ill-posed in the sense of Hadamard,[35] the automatic regularization procedure proposed by Zamponi[36] has been employed. The sound propagation from each potential source to every listener location, i.e., every microphone, is modeled using the free-field Green's function. Three different types of sources have been predefined as
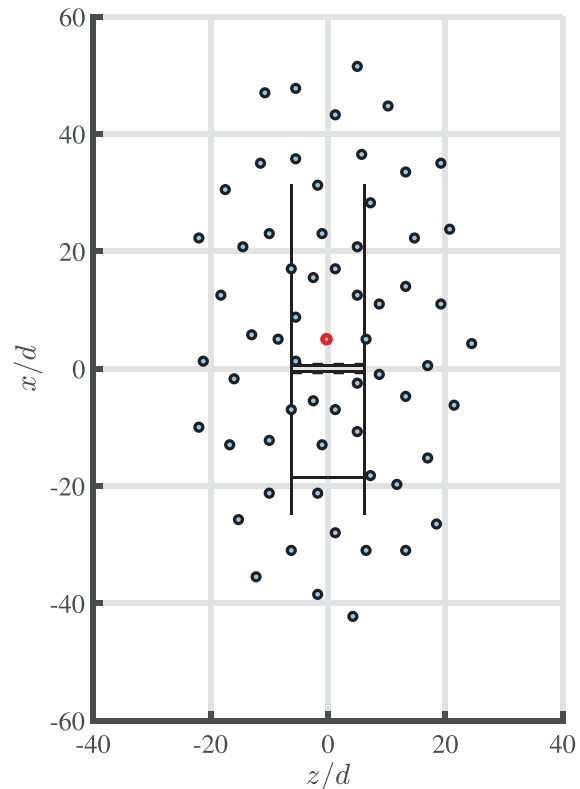

FIG. 4. Relative position of the microphone array and the test section. The black lines indicate side plates, nozzle exit, and cylinder leading edge and trailing edge. The central microphone of the array is highlighted in red.

reference solutions, i.e., a monopole and dipoles aligned both in the x and y directions, hence linearly independent. In this way, dipolar source contributions oriented in an arbitrary direction on the x–y plane can be identified by their linear combination.[32]

The scanning grid for evaluating the potential sources varies between $-25 < z/d < 25$ and $-25 < x/d < 25$, with a spatial resolution of $0.25\,d$, and is centered at the origin of the reference system. The extension of the grid can be visualized in Fig. 5, which illustrates the point-spread function (PSF)[37] of the array for a synthetic monopolar source located at the origin and emitting white noise at the one-third-octave frequency band of $f_{1/3} = 1.6$ kHz. The PSF is characterized by an axial symmetry concerning the x and z axes and features a higher resolution along x, making the microphone arrangement suitable to separate noise sources in the flow direction. Moreover, corrections to account for the convection of the mean flow and refraction of the shear layer have been applied following the method proposed by Sijtsma,[38] whereas measurements of the test section without the cylinder configurations have been performed to account for the background noise of the wind tunnel.

IV. RESULTS AND DISCUSSION
A. Sound pressure levels

The sound-pressure levels L_p of the signal computed with a reference pressure of $p_{ref} = 20\ \mu$Pa and acquired by the central microphone
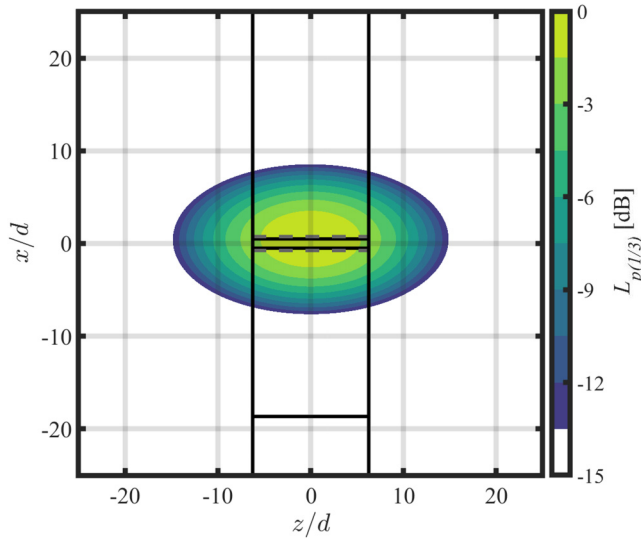
FIG. 5. Point-spread function at $f_{1/3} = 1.6$ kHz for a simulated source emitting white noise at the origin of the coordinate system. The flow goes from the bottom to the top of the map.
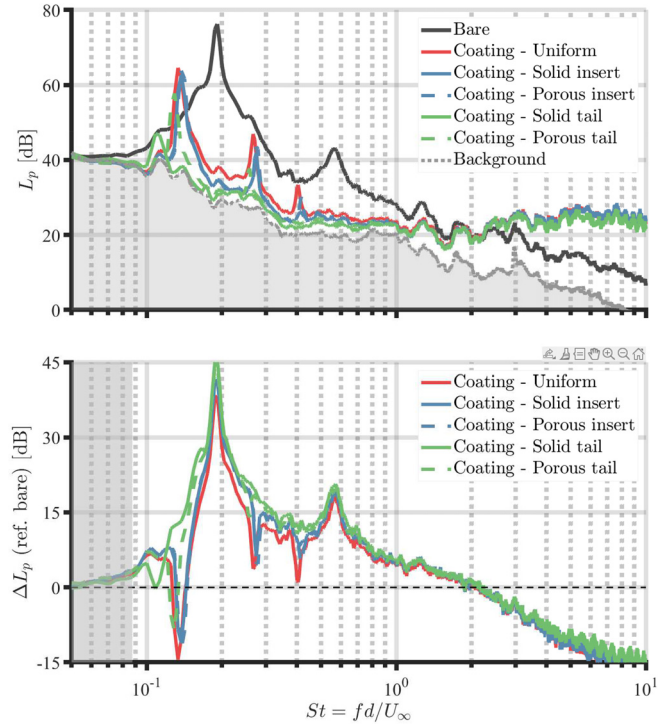

FIG. 6. Absolute and relative (with respect to the baseline) sound pressure levels for the bare cylinder and the cylinder configurations with the porous coating [right-hand group in Fig. 3(a)] at $Re_d = 4.1 \times 10^4$ measured by the central microphone of the array and computed with a reference pressure of $p_{ref} = 20$ μPa. The gray-tinted area on the bottom figure denotes the region in which the signal-to-noise ratio for the baseline is lower than 3 dB.

of the array, which is placed at an observation angle of approximately $\pi/2$ with respect to the stagnation streamline, are plotted in Fig. 6 for the cylinder configurations including the metal-foam coating [right-hand group in Fig. 3(a)]. The frequency spectra are presented in function of the Strouhal number based on d and U_∞ and refer to $Re_d = 4.1 \times 10^4$, but the same conclusions can also be extended to the other free-stream Reynolds numbers since the sound-reduction trends have been observed to be mostly independent of the flow speed.

Consistent findings with Zamponi et al.[22] are obtained for the baseline and the cylinder uniformly coated with the metal foam: the porous treatment is effective in mitigating noise. The difference in the outer diameter yields a shift of the tonal peak linked to the vortex shedding toward lower frequencies and substantial attenuation of its amplitude. The resulting peak-to-peak reduction amounts to about 11 dB at the vortex-shedding frequency, as reported in Table II, which, for the baseline, occurs at $St = 0.185$ and is in agreement with previous measurements involving circular cylinders tested in the same experimental setup.[39,40] An effective diameter of $D_{eff} = 0.950 D$ would be required to achieve the same result for the porous configuration. Concerning the broadband-noise range, a significant reduction of up to approximately 10 dB is found. However, the aeroacoustic benefit of the coating reduces with increasing frequency due to the occurrence of noise induced by the inner turbulent flow interacting with the struts of the open-cell metal foam.[22] The transition between sound decrease and

increase takes place at $St \approx 2$, while, at $St \approx 10$, the noise increment is estimated to be about 15 dB, independently of the tested geometry.

Overall, the presence of the insert [see Fig. 3(a)] results in an additional noise decrease in up to 4 dB in the broadband range, especially in the region between the vortex-shedding peak and its first harmonic. This trend can be better visualized in Fig. 7, which depicts the relative sound pressure levels of the modified coated configurations with respect to the uniform cover. No notable difference between the solid and porous inserts is found, possibly due to the fact that the perforations are oriented normally to the streamwise direction in the leeward part of the coating, in a region where the flow is expected to be partially separated, and have a negligible effect on the flow ejection in the near-wake region. At high frequencies, the sound-increase trend overlaps with that of the uniform coating, hinting that noise due to the turbulent-flow interaction within the pores is generated on the metal-

TABLE II. Peak-to-peak noise reductions evaluated at the vortex-shedding frequency for the different cylinder configurations in Fig. 3(a) with respect to the baseline.

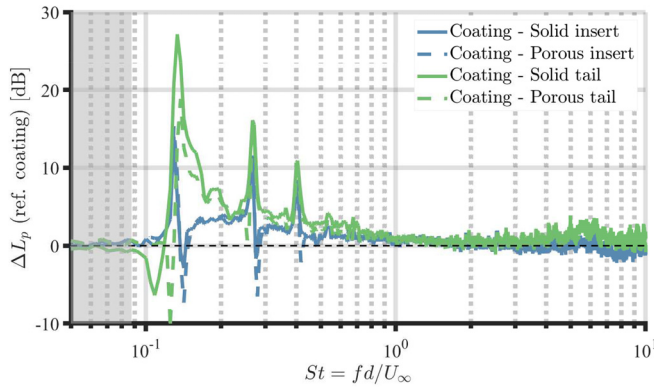| Cylinder	Coating	Coating	Coating	Coating	Coating	Bare	Bare	Bare	Bare
Configuration	Uniform	Solid insert	Porous insert	Solid tail	Porous tail	Solid insert	Porous insert	Solid tail	Porous tail
$\Delta L_{p_{vs}}$ (dB)	10.76	12.55	11.98	29.22	17.51	12.16	12.42	19.04	17.79

FIG. 7. Relative (with respect to the uniformly coated cylinder) sound pressure levels for the cylinder configurations with the porous coating [right-hand group in Fig. 3(a)] at $Re_d = 4.1 \times 10^4$ measured by the central microphone of the array. The gray-tinted area on the bottom figure denotes the region in which the signal-to-noise ratio for the baseline is lower than 3 dB.

foam surface in the front part of the body and is, therefore, not affected by the modifications in the back.

When the tail is integrated into the porous cover, the aeroacoustic performance of the treatment considerably improves (Fig. 6). With the porous configuration, consistent mitigation of up to 10 dB is achieved for the broadband-noise range ($St < 1$). Moreover, the high-frequency sound increase for $St > 2$ is slightly attenuated. Such trends are even more emphasized when the coated cylinder is fitted with a solid tail. In this case, the peak-to-peak reduction at the vortex-shedding frequency amounts to approximately 18.5 dB with respect to the uniform coating, which, in turn, leads to a decrease in about 29.2 dB if compared with the bare configuration, as indicated in Table II. In addition, the sound pressure levels for this configuration for $St < 0.2$ are dominated by the background noise of the facility, suggesting that its sound-control potential in comparison with the baseline may be even greater in this frequency range. Interestingly, the Strouhal number at which the vortex shedding occurs is shifted toward lower frequencies, yielding $D_{eff} = 1.175 D$. The presence of a solid plane that guides the flow ejected by the porous coating is most likely able to stabilize further the cylinder wake and increase its width, motivating the larger effective diameter.

The results shown above demonstrate that a nonuniform coating effectively reduces aerodynamic noise. Nevertheless, integrating a flow-permeable cover is not indispensable to achieving this effect. As illustrated in Fig. 8, consistent sound attenuation is obtained even when the inserts and tails are fitted to the cylinder in the absence of the metal-foam cover [left-hand group in Fig. 3(a)]. With the former, a ΔL_p of approximately 10 dB for $0.1 < St < 0.6$ and around 5 dB for $St > 0.6$ is achieved. Similar to the previous case, no significant difference between the solid and porous insert configurations can be found, even in the noise-to-noise peak mitigation (see Table II). In contrast, the presence of perforations in the latter considerably affects the noise levels produced by the flow past the cylinder. On the one hand, the porous tail provides higher sound reductions in the vicinity of the aeolian tone than the inserts but worse performance in the high-frequency range, especially for $St > 1$, probably due to the flow recirculating within the perforations of the 3D-printed component.[41] This effect has
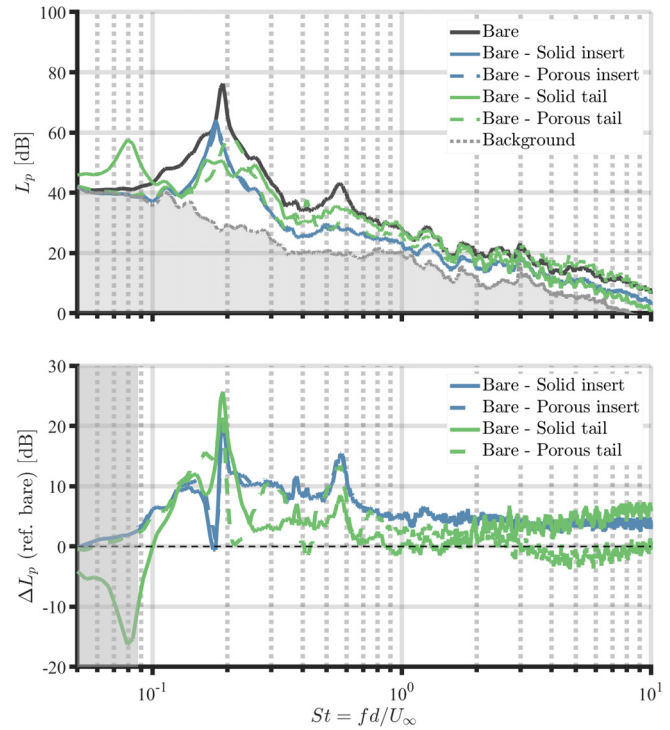

FIG. 8. Absolute and relative (with respect to the baseline) sound pressure levels for the bare cylinder and cylinder configurations without the porous coating [left-hand group in Fig. 3(a)] at $Re_d = 4.1 \times 10^4$ measured by the central microphone of the array and computed with a reference pressure of $p_{ref} = 20 \ \mu Pa$. The gray-tinted area on the bottom figure denotes the region in which the signal-to-noise ratio for the baseline is lower than 3 dB.

been observed to be more prominent for lower velocities. On the other hand, the solid tail substantially shifts the vortex-shedding peak toward lower Strouhal numbers, leading to a significant peak-to-peak tonal decrease in approximately 19 dB and hinting at an alteration in the flow physics associated with this configuration. Further details about this mechanism will be given in Sec. IV C.

Integrating the L_p spectra over the frequency can impart a more complete picture of the aeroacoustic impact of the different cylinder configurations in Fig. 3(a). The overall sound pressure level L_{p_O} is computed as the integral of the power spectral density of the acoustic pressure measured by the central microphone of the array. In this case, the integration is performed between $f = 131.25$ Hz, which represents the threshold above which the sound radiated by the bare cylinder for $Re_d = 4.1 \times 10^4$ overcomes the background noise by at least 3 dB (gray-tinted regions in Figs. 6–8), and $f = 20$ kHz, i.e., the upper limit of the audible hearing range.

The L_{p_O} results are illustrated in Fig. 9. The uniform coating provides an overall reduction of about 12 dB with respect to the baseline, which represents a trade-off between the substantial noise decrease at low frequencies and the significant noise increase at high frequencies. The presence of the inserts leads to further attenuation of approximately 2 dB, confirming the conclusions previously drawn. The incorporation of the tails in the metal-foam cover results in the most promising aeroacoustic performance, amounting to additional 9 and
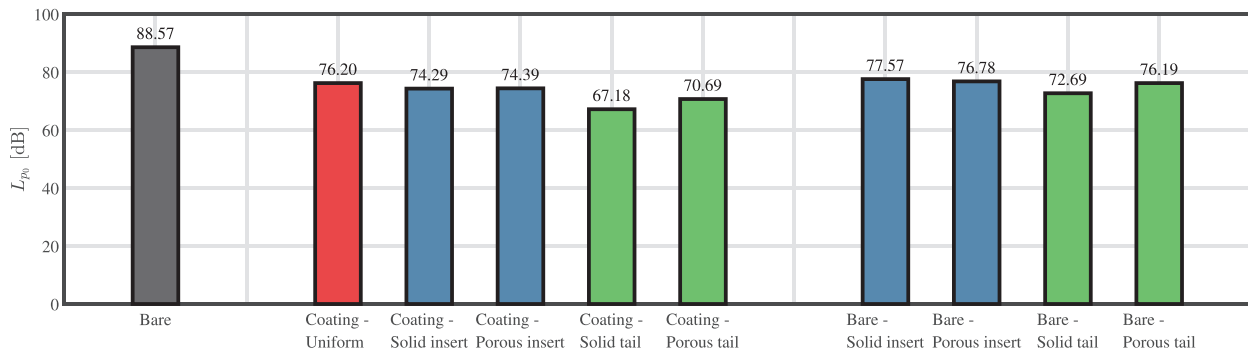
FIG. 9. Overall sound pressure level for the different cylinder configurations at $Re_d = 4.1 \times 10^4$ integrated between $f = 131.25$ and $f = 20000$ Hz. The L_{p_O} values are indicated at the top of each bar. The notation for each cylinder configuration refers to Fig. 3(a).

5.5 dB of L_{p_O} mitigation, if compared to the uniform coating, for the solid and porous tail, respectively. It is important to stress that the values mentioned above constitute a conservative estimation of the sound-reduction potential of this technology since, for the initial part of the spectrum considered in the integration, i.e., for $St < 0.15$, the background noise dominates over the sound radiated by the coated cylinders. This observation is especially valid for the cover integrated with the solid tail, for which the signal-to-noise ratio is mostly below 3 dB up to $St \approx 0.2$.

Interestingly, a comparable sound-control performance is achieved for the cylinder configurations without the metal-foam cover, most likely because the decrease in L_{p_O} is not hindered by the high-frequency noise increase occurring with the cover. The incorporation of the solid and porous inserts and the porous tail in the leeward part of the body results in a similar ΔL_{p_O} with respect to the baseline of 11–12 dB. Likewise, these values do not account for the dominance of the background noise for $St < 0.15$. Conversely, the bare cylinder with the solid tail grants the best overall sound reduction, which amounts to 15.9 dB. Yet, the high energy content associated with the tonal peak at $St \approx 0.08$ is not taken into consideration in this case since it lies outside the integration range for the L_{p_O} computation. This contribution is expected to considerably worsen the noise-mitigation efficiency related to this configuration.

B. Noise-spectra scaling

The L_p trends presented so far suggest that the modified coatings of the cylinder are able to enhance the physical effect responsible for noise mitigation. To shed light on the nature of the generated sound sources, the frequency spectra presented at a reference distance of 1 m are scaled with the sixth power of U_∞, which is known to be related to a dipolar sound directivity.[18] The results are reported in Figs. 10 and 11 for the modifications in the presence and absence of the porous coating, respectively. For the former, a good collapse of the sound-pressure levels is found for all the cylinder configurations and for most of the frequency spectrum, in agreement with the outcomes of the scaling analysis carried out by Zamponi et al.[22] on the baseline and the cylinder uniformly coated with the 10 PPI metal foam. Similar findings are obtained when the solid and porous inserts are connected to the bare cylinder [Figs. 11(a) and 11(b)], suggesting that the noise-generation mechanism is unchanged. Moreover, the lack of collapse at

$St > 6$ for the coated cylinder configurations confirms the theory that another sound-production process starts dominating at higher frequencies, i.e., that associated with the turbulent-flow interaction within the pores of the permeable cover. The non-compactness of the cylinder in this frequency range is also expected to contribute to the failure in the proposed scaling with the flow speed. A better collapse seems to be reached for a lower exponent, in the order of 4–4.5, although further analyses would be required to assess the nature of this noise source.

The outcome of this investigation confirms that sound waves acquired by the microphone are those scattered by the cylinder surface, which, as mentioned in Sec. II and confirmed by Eq. (8), feature dipolar directivity. In this regard, Zamponi et al.[15] showed that the nature of the far-field sound depends on the observation angle where the microphone lies and the relative contribution of the acoustic field directly radiating from the volume sources in the wake, i.e., p'_d [first term in the right-hand side of Eq. (6)], and that diffracted by the body, i.e., p'_s [second term in the right-hand side of Eq. (6)]. For the angles normal to the streamwise direction, the scattered field dominates, even for the coated-cylinder configurations, since the radiation efficiency of p'_s is maximum and that of p'_d is minimum. This explains why the aerodynamic noise scales with the U_∞^6 at the observation angle defined by the central microphone of the array, supporting the scenario pictured above.

However, the same trend is not maintained when the tails are integrated into the baseline design. For these configurations, the optimal scaling factor of the sound spectra with respect to the flow velocity seems to differ from the sixth power, especially in the medium-to-high frequency range. This change can be better visualized in Fig. 12, which depicts the evolution of the overall sound-pressure level over the free-stream Reynolds number. The integration of the spectra has been performed for $St > 0.5$ to investigate the broadband-noise range of the frequency spectra. The results feature a L_{p_O} dependency closer to U_∞^5 than U_∞^6, suggesting that the noise may be produced by the scattering of the turbulent boundary layer at the trailing edge of the tail.[42] Indeed, the sound radiated by a turbulent flow interacting with a surface is more efficient in the presence of a geometrical singularity. Such a hypothesis confirms the observations made in Sec. III C at the basis of the different noise-production mechanisms linked to the tail design and will be better investigated in Sec. IV C.
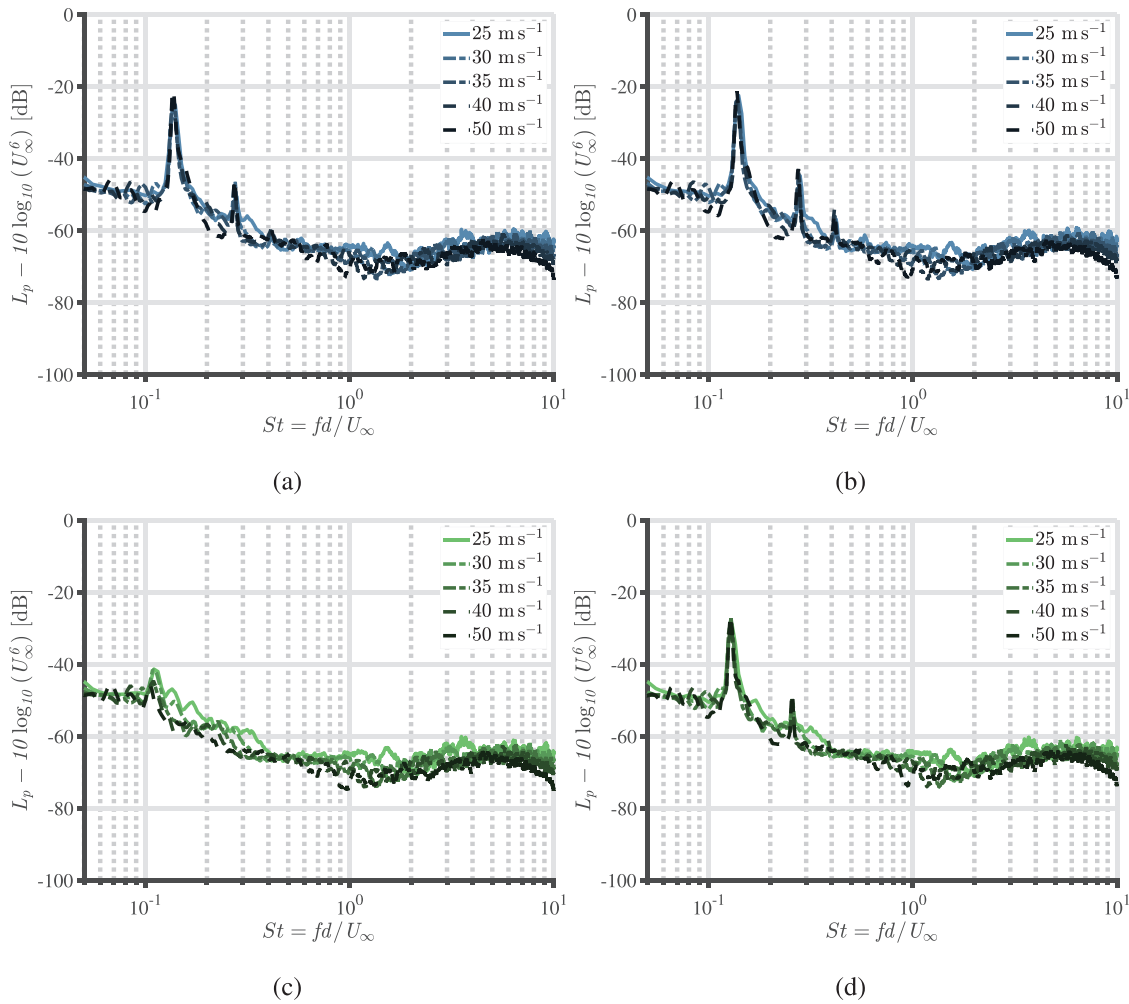
02 January 2024 12:36:44

FIG. 10. Sound pressure levels at different free-stream flow velocities for the coated cylinder integrated with the (a) solid insert, (b) porous insert, (c) solid tail, and (d) porous tail measured by the central microphone of the array and computed with a reference pressure of $p_{ref} = 20 \ \mu$Pa. The spectra are scaled with the sixth power of the flow velocity.

C. Sound-source visualization

Further insight into the noise-reduction mechanism due to the innovative cylinder coatings is provided by the source-distribution maps computed with the GIB in Figs. 13, 15, and 16. The results are evaluated at a one-third octave frequency band of $f_{1/3} = 1.6$ kHz and free-stream Reynolds number of $Re_d = 6.8 \times 10^4$, which yield a Strouhal number based on d of $St = 0.64$, lying in the broadband-noise range of the frequency spectrum. This frequency was chosen because it represents a compromise between ensuring an acceptable spatial resolution of the sound maps and avoiding the occurrence of noise due to the turbulent-flow interaction within the pores. The findings discussed in this subsection can be generalized to the frequencies below the previously mentioned threshold and the different free-stream flow velocities, as demonstrated by Zamponi *et al.*[15] Moreover, only the monopole part of the reconstructed acoustic field will be displayed for all the maps presented below since it dominates over the other source contributions. This is a consequence of the 2D micro-phone distribution of the array employed in the study and will be addressed in more detail in the Appendix.

Before proceeding with the analysis of the results, it is crucial to specify that inverse beamforming techniques, including the GIB, display the source-distribution contours rather than the peak-source intensity, in contrast with direct methods.[32] Therefore, integrating the sound maps is required to quantitatively assess the source strength, which clarifies the relatively low noise levels indicated in the figures.

Furthermore, the following considerations should be made to better interpret the outcome of this investigation:

- The source-receiver propagation model implemented in the GIB beamforming algorithm is based on the free-field Green's function, as explained in Sec. III D. Hence, two sources are expected to simultaneously appear in the sound maps, i.e., the volume sources in the wake radiating the direct acoustic field p'_d and the
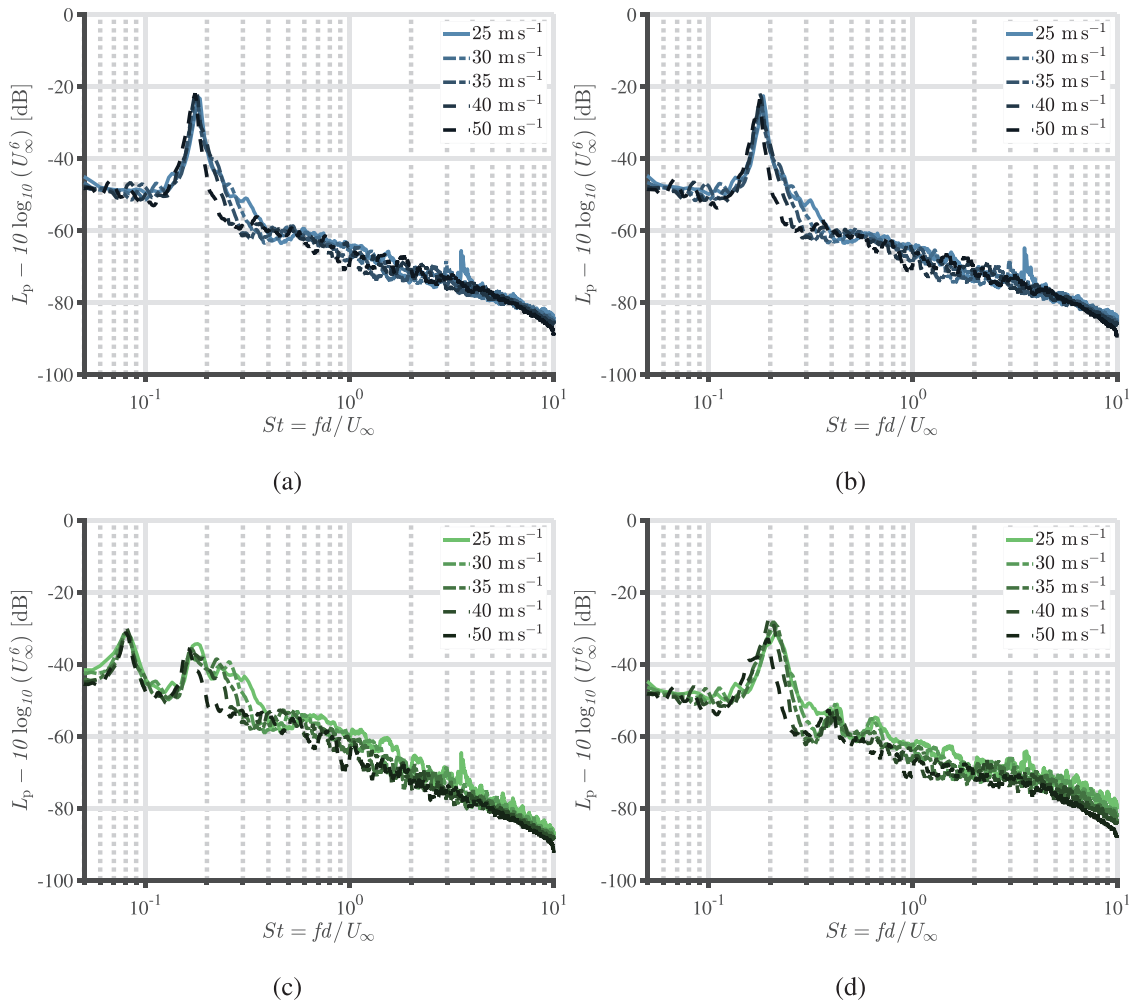
FIG. 11. Sound pressure levels at different free-stream flow velocities for the bare cylinder integrated with the (a) solid insert, (b) porous insert, (c) solid tail, and (d) porous tail measured by the central microphone of the array and computed with a reference pressure of $p_{ref} = 20\ \mu$Pa. The spectra are scaled with the sixth power of the flow velocity.

image sources that result from the sound scattered by the cylinder surface p'_s. Nevertheless, their strength is determined by the relative contribution of the two acoustic fields in the geometric far field, which, in turn, establishes whether the two noise-source distributions are included within the same dynamic range in the maps.[15]

- As mentioned in Sec. II B, the efficiency of the diffraction mechanism, which depends on the amplitude of the image source, exponentially reduces with the increasing distance between the vortex-shedding onset and the surface, i.e., for larger vortex-formation lengths, and increasing frequencies due to non-compactness effects.

- The position of the image source is linked to the location of the quadrupole in the wake: the shorter the distance of the latter from the surface is, the closer the two source contributions will be as a consequence of the circle theorem.[43] At $f_{1/3} = 1.6$ kHz, the resolution of the beamforming output may still be insufficient to adequately separate their noise contributions. In the cases in

which the physical and image sources are included within the same dynamic range, only one source incorporating the two contributions will be displayed.

In view of the above, the results for the baseline and the uniformly coated cylinder (Fig. 13) confirm the conclusions that were drawn in the previous study:[15] the integration of a flow-permeable cover leads to a substantial L_p decrease, in accordance with the frequency spectra in Fig. 6, and a significant downstream shift of the dominant source distribution, which moves from the cylinder surface to the wake, precisely at the onset position of the shedding instability. Both sound mitigation and source displacement agree with the previous findings. For the baseline, the sound map most probably comprises only the image source, i.e., the origin of the scattered field. Conversely, for the coated configuration, the strength of the image source is likely not included in the dynamic range of the map due to the increased vortex-formation length. Hence, only the volume sources in the wake are visible. A more in-depth analysis of the present results using the
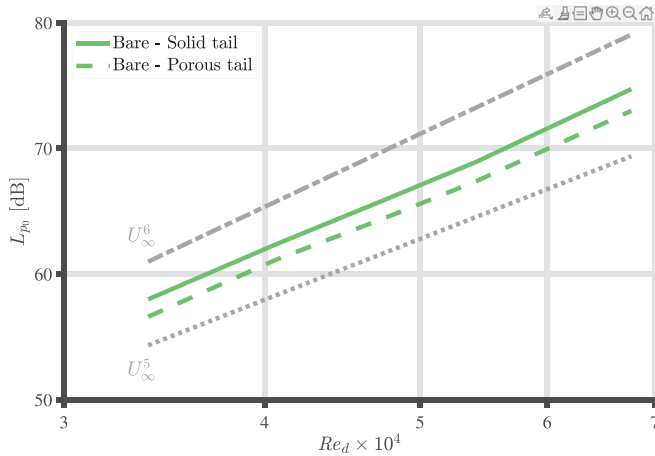
FIG. 12. Overall sound pressure levels at different free-stream Reynolds numbers for the bare cylinder integrated with the solid and porous tail measured by the central microphone of the array and computed with a reference pressure of $p_{ref} = 20\ \mu$Pa. The integration is performed in the broadband-noise range of the frequency spectrum, for $St > 0.5$. The slopes associated with the fifth and sixth powers of the flow speed are also indicated in the plot.

multipole-detection capabilities of the GIB technique is provided in the Appendix.

The correspondence between the quadrupole location and the outbreak of the vortex shedding can be better visualized in Fig. 14, where the sound map in Fig. 13(b) is superimposed to the contour map of the turbulence kinetic energy k computed from the PIV data of Zamponi et al.[15] The peak of this statistical flow parameter, which corresponds to the end of the wake recirculation region where the vortical eddies detach from the shear layers and begin their oscillatory movement, coincides with the origin of the dominant noise sources. Such a

result further corroborates the physical considerations made in Sec. II B about the nature of cylinder flow-induced noise and the sound-mitigation mechanisms of the porous coating, which are at the basis of the proposed innovative modifications.

The same trend analyzed for the uniform porous cover characterizes the coated cylinders integrated with the inserts and tails in Fig. 15. Notably, the configurations that provide the best noise reductions also feature the largest downstream shift of the quadrupolar source in the wake, as can be better visualized in Table III, which includes the streamwise locations of the dominant sound sources extracted by the corresponding sound maps in Figs. 13, 15, and 16. This finding confirms the assumptions at the basis of the innovative covers described in Sec. III B, as well as the noise-attenuation mechanism connected with this technology. Indeed, the more streamlined internal flow within the porous medium likely contributes to further stabilizing the flow past the cylinder, delaying the onset of the shedding instability and, therefore, decreasing the efficiency of the sound diffracted by the body.

Likewise, similar observations can be made for the baseline with the solid [Fig. 16(a)] and porous [Fig. 16(b)] inserts, although this modification yields a smaller displacement (Table III) and, hence, lower sound mitigation in this frequency band, as seen in Fig. 8. In comparison with the bare cylinder in Fig. 13(a), the efficiency of the diffraction mechanism is reduced, and the maps display the volume sources in the near wake as well as the image source on the surface as a unique source distribution located over the leeward part of the body.

In contrast, the sound-source distributions are approximately centered at the trailing-edge level of the 3D-printed components for the two configurations in which the tails are integrated into the baseline [Figs. 16(c) and 16(d)], corroborating the hypotheses made in Sec. IV B about the nature of the radiated sound. The location of the dominant source distributions in the maps is indeed consistent with those of Geyer et al.,[44] who applied phased-array techniques to characterize the trailing-edge noise radiated by solid and porous airfoils. In
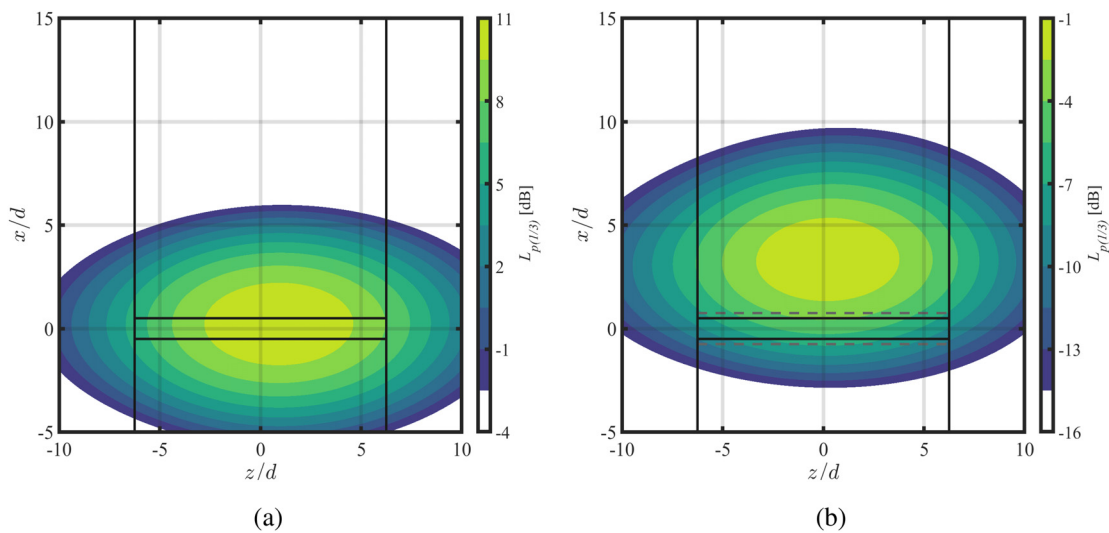

FIG. 13. GIB source-distribution maps for (a) the baseline and (b) the cylinder uniformly coated with metal foam at $f_{1/3} = 1.6$ kHz and $Re_d = 6.8 \times 10^4$ ($St = 0.64$) computed with a reference pressure of $p_{ref} = 20\ \mu$Pa.
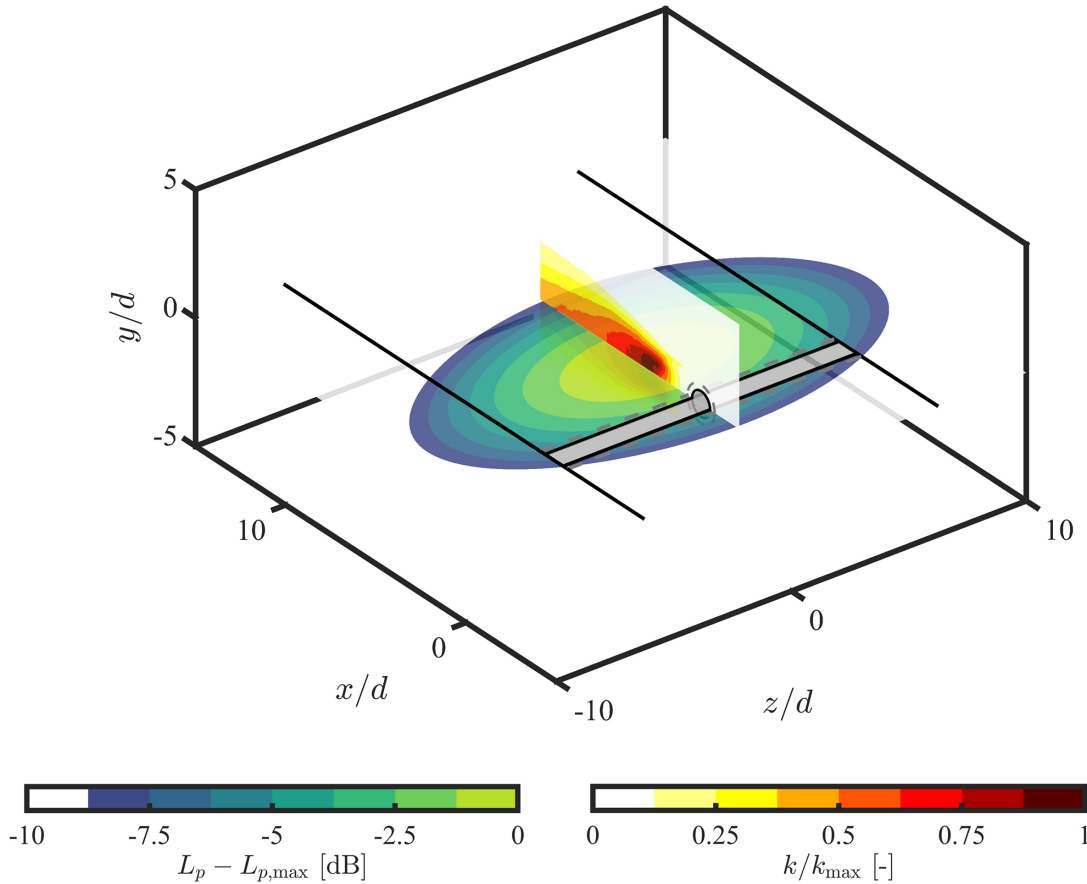
FIG. 14. GIB source-distribution map at $f_{1/3} = 1.6$ kHz and turbulence kinetic energy contour for the uniformly coated cylinder at $Re_d = 6.8 \times 10^4$. The maps are normalized by the corresponding maximum values. PIV data from Zamponi et al.[15]

this case, the noise mitigation may be associated more with the more streamlined shape of the body, which is expected to affect the flow separation and near-wake development, rather than the alteration of the sound diffraction. In other words, the modified cylinder acts similarly to a thick airfoil, as speculated in Sec. III C, and the improved aeroacoustic performance of the porous tail at low frequencies may be related to the flow communication within the pores of the material.[45] In addition, a considerable displacement toward positive z/d is found for the solid tail [Fig. 16(c)], which may be linked to a potential non-homogeneity in the 3D-printed material. Further flow field investigations will be required to elucidate the origin of this mechanism and

also the significant vortex-shedding displacement toward lower frequencies in Fig. 11, which remains an open question.

V. CONCLUDING REMARKS

This study demonstrates that an exhaustive understanding of the sound-reduction mechanisms of a porous-coated cylinder can result in novel technological solutions for abating the corresponding flow-induced noise. In particular, the alteration of the sound diffraction serves as a viable control mechanism for attaining this objective. Inexpensive and light modifications of a flow-permeable cover, in the form of inserts or tails integrated into the porous material, are shown

TABLE III. Streamwise position of the dominant noise sources extracted from the beamforming sound maps at $f_{1/3} = 1.6$ kHz and free-stream Reynolds number of $Re_d = 6.8 \times 10^4$ for the different cylinder configurations in Fig. 3(a). The uncertainty linked to source localization amounts to $\pm 0.125\,d$ due to the spatial resolution of the scanning grid.

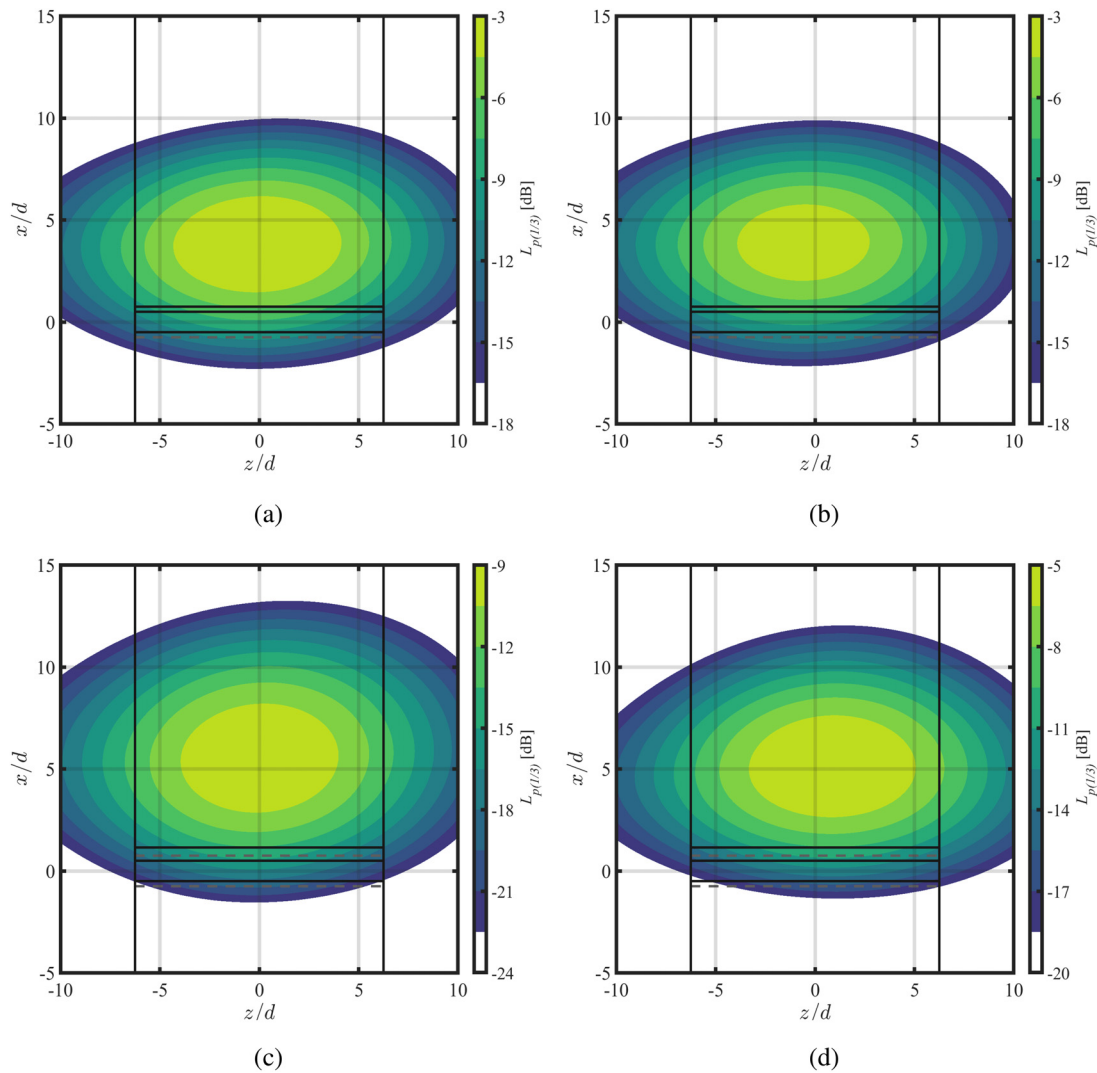| Cylinder	Coating	Coating	Coating	Coating	Coating	Bare	Bare	Bare	Bare
Configuration	Uniform	Solid insert	Porous insert	Solid tail	Porous tail	Solid insert	Porous insert	Solid tail	Porous tail
x/d	3.25	4	3.75	5.5	5	1.25	1.25	1.25	1.25

FIG. 15. GIB source-distribution maps for the cylinder coated with metal foam and integrated with the (a) solid insert, (b) porous insert, (c) solid tail, and (d) porous tail at $f_{1/3} = 1.6$ kHz and $Re_d = 6.8 \times 10^4$ ($St = 0.64$) computed with a reference pressure of $p_{\text{ref}} = 20 \ \mu$Pa.

to yield additional attenuation of up to 10 dB with respect to a uniform coating throughout the frequency spectrum, leading to an Aeolian-tone decrease in up to about 29 dB if compared with the baseline. The experimental findings confirm that the aerodynamic noise radiated by the flow past a cylinder is dominated by the scattering of the quadru-polar source originating at the vortex-shedding onset location by the body surface, which is dipolar in nature. The farther from the surface this position is, the less efficient the sound diffraction will be. This physical mechanism is at the basis of the noise reduction achievable by the porous coating of a cylinder.

The presence of a component in the leeward part of the cover that better guides the internal flow around the body leads to a further downstream displacement of the shedding-instability outbreak, i.e., better sound mitigation. In some instances, such as when the solid tail is integrated into the porous coating, the tonal peak associated with the

vortex shedding in the noise spectra is found to be almost completely suppressed. Despite the promising results, no optimization of these modifications has been attempted yet, leaving considerable room for improvement of their noise-control potential. In this regard, the recent advancements in additive-manufacturing techniques can offer the per-fect framework for designing nonuniform porous covers that are able to enhance the downstream source shift.

Interestingly, a significant attenuation of up to 10 dB in compari-son with the baseline is also obtained when the same components are connected to the cylinder, without the presence of the porous layer. In this case, the mitigation of overall sound pressure levels is similar to that generated by the coated configurations owing to the lack of high-frequency noise increase due to the turbulent-flow interaction within the metal-foam pores. For the inserts, the sound decrease is induced by the same mechanism described above, whereas, for the tails, it is linked
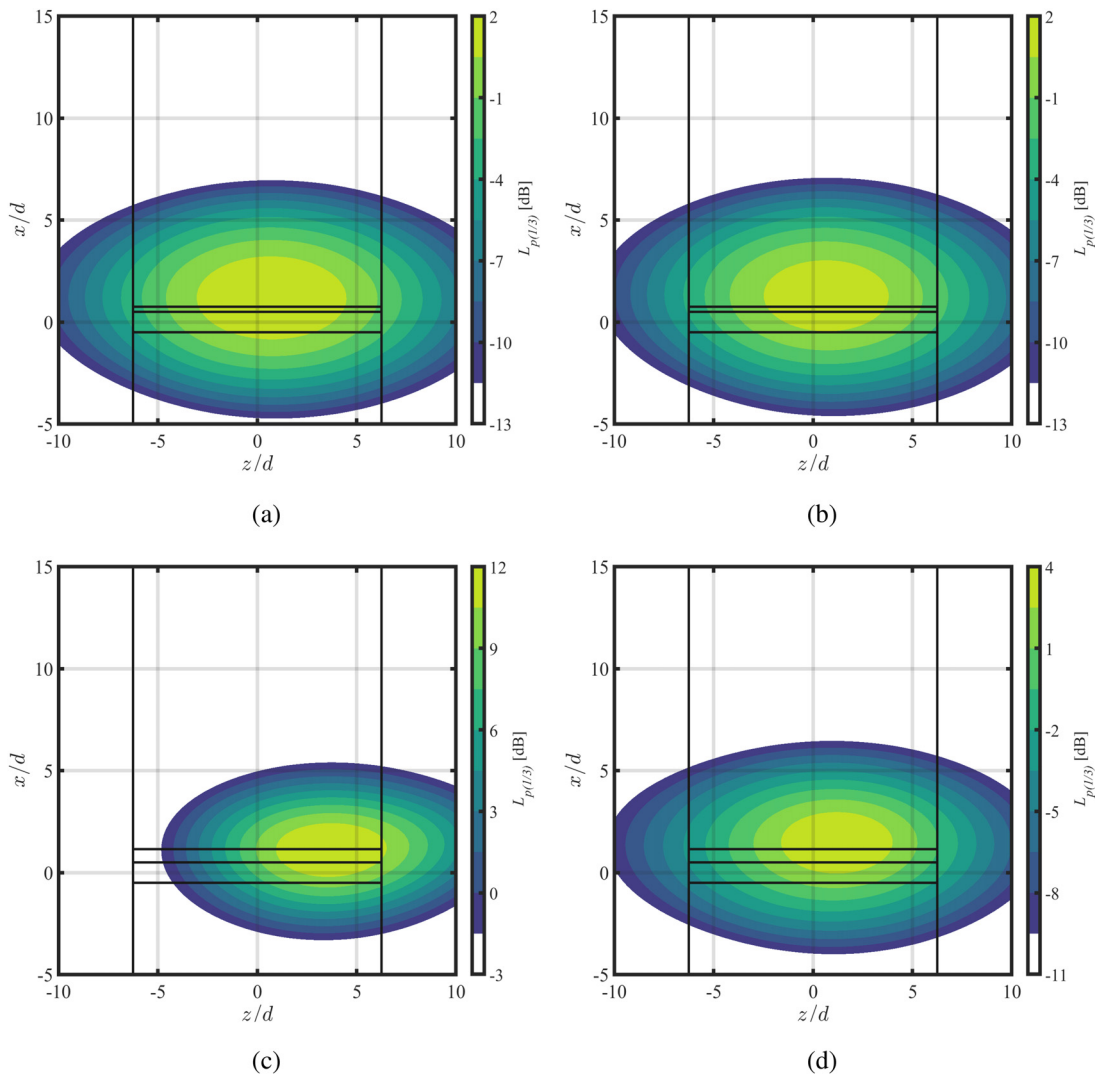
FIG. 16. GIB source-distribution maps for the bare cylinder integrated with the (a) solid insert, (b) porous insert, (c) solid tail, and (d) porous tail at $f_{1/3} = 1.6$ kHz and $Re_d = 6.8 \times 10^4$ ($St = 0.64$) computed with a reference pressure of $p_{\mathrm{ref}} = 20$ μPa.

to the more streamlined shape of the body that makes the modified cylinder act as a thick airfoil, like the scaling analyses of the sound spectra with respect to the flow speed demonstrate. This outcome additionally hints at an optimal extension for the insert to allow the alteration of the sound diffraction to occur.

Although the noise-control performance of this component is inferior to that achievable using a flow-permeable coating in the low-frequency range, its technological potential is vast. As this research demonstrates, integrating an insert into the leeward side of the cylinder leads to a significant and consistent aerodynamic-sound reduction for the whole frequency spectrum, contributing to the L_{p_O} attenuation shown in Fig. 9. From an engineering perspective, this solution enables overcoming practical issues that porous media may face in operating conditions, e.g., their susceptibility to environmental elements, such as

moisture absorption or clogging. These factors, as well as long-term durability concerns due to degradation, potentially impair the effectiveness of flow-permeable materials by increasing their effective resistivity. Consequently, the overall sound-control performance of a porous coating might be lower than that obtained in the laboratory experiments discussed in the paper. On the contrary, the modifications directly connected to the bare cylinder constitute a more robust solution to environmental factors. As long as the incidence of the flow interacting with the bluff body remains consistent with the designed one, it is reasonable to expect sound-pressure-level reductions of up to 10 dB for $0.1 < St < 0.5$ also in practical applications. In addition, the stabilization effect that this modification yields, combined with the absence of a porous cover that enlarges the wake width, may also result in a significant decrease in the drag force produced by the body,

opening interesting scenarios for different industrial applications. The application of flow-visualization techniques to the existing setup could shed light on this beneficial aspect and will constitute a topic for future work.

ACKNOWLEDGMENTS

AUTHOR DECLARATIONS
Conflict of Interest

The authors have no conflicts to disclose.

Author Contributions

Riccardo Zamponi conceived the study, designed the experiments, conducted the research, and analyzed the data. Francesco Avallone and Daniele Ragni provided critical feedback on the experimental methods and data analysis. Sybrand van der Zwaag was responsible for acquiring funding for the project and assisted in the design of the cylinder coatings. All authors have read and approved the final manuscript.

Riccardo Zamponi: Conceptualization (lead); Data curation (lead); Formal analysis (lead); Investigation (lead); Methodology (lead); Software (lead); Validation (lead); Visualization (lead); Writing – original draft (lead). **Daniele Ragni:** Funding acquisition (equal); Investigation (supporting); Supervision (equal); Writing – review & editing (equal). **Sybrand van der Zwaag:** Funding acquisition (equal); Supervision (equal); Writing – review & editing (equal). **Francesco Avallone:** Formal analysis (supporting); Investigation (supporting); Supervision (equal); Writing – review & editing (equal).

DATA AVAILABILITY

The data that support the findings of this study are available from the corresponding author upon reasonable request.

APPENDIX: MULTIPOLE DETECTION

The capability of the GIB to detect multipole sources offers an ulterior opportunity to investigate the nature of the equivalent noise sources produced by the flow past the cylinders. This technique, however, is limited by the planar microphone distribution employed in the present research. The resolvable multipole components are indeed constrained to the target plane-parallel to the microphone array, and multipoles that are oriented toward the array direction are predominantly detected as monopoles,[32] as mentioned in Sec. IV C. Nevertheless, although they are characterized by smaller source strengths, the sound maps relative to the different dipole components can still be analyzed to reveal the radiation pattern of these sources in a qualitative manner.

Figures 17 and 18 depict the GIB sound maps of the dipoles oriented along x and y for the baseline and the cylinder uniformly coated with the metal foam, respectively. The same dynamic range of 30 dB has been imposed to ease the visualization of the relative contributions of the two categories of equivalent sources. For the bare cylinder, the acoustic energy is mainly produced by the dipole with the axis perpendicular to the scanning grid [Fig. 17(a)], which features a similar source distribution to the sound map of the monopolar component [Fig. 13(a)]. In contrast, the noise sources for the dipole oriented along x exhibit two low-amplitude peaks equidistant to the actual source
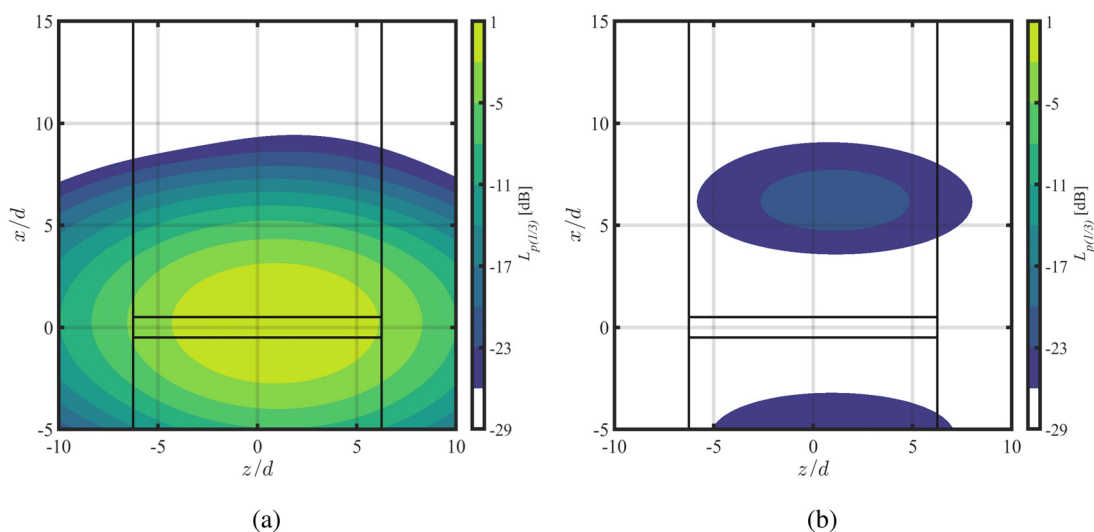

FIG. 17. Dipolar components of the GIB source-distribution maps for the baseline at $f_{1/3} = 1.6$ kHz and $Re_d = 6.8 \times 10^4$ ($St = 0.64$) computed with a reference pressure of $p_{ref} = 20\ \mu$Pa: (a) dipole oriented along y; (b) dipole oriented along x. The same dynamic range is imposed for both maps.
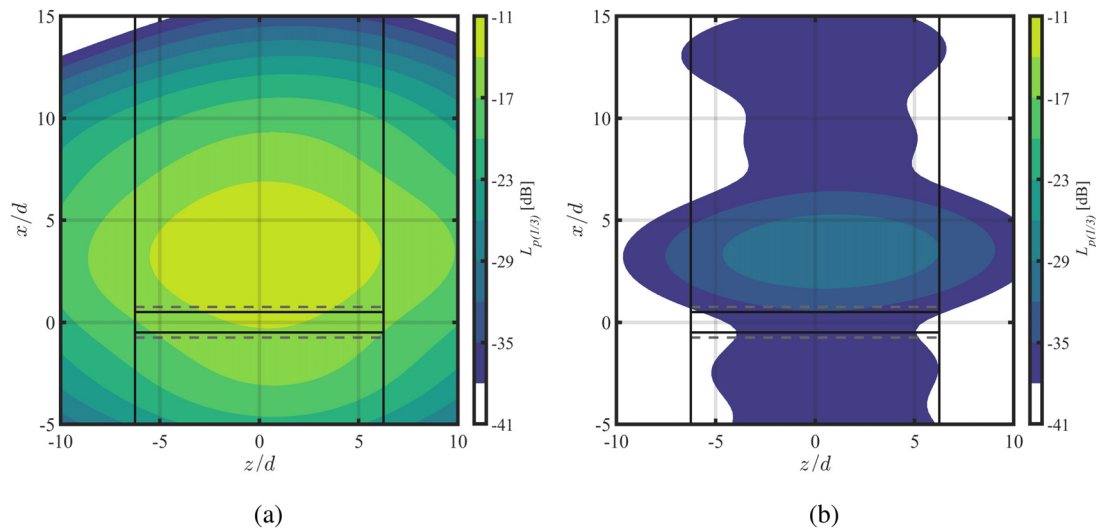
FIG. 18. Dipolar components of the GIB source-distribution maps for the cylinder uniformly coated with metal foam at $f_{1/3} = 1.6$ kHz and $Re_d = 6.8 \times 10^4$ ($St = 0.64$) computed with a reference pressure of $p_{ref} = 20$ μPa: (a) dipole oriented along y; (b) dipole oriented along x. The same dynamic range is imposed for both maps.

location and aligned with the dipole axis [Fig. 17(b)]. A similar spurious effect is obtained when a dipole whose axis is parallel to the microphone array is resolved using a monopole as a reference source.[32]

The situation differs for the dipolar components of the GIB sound maps for the coated configuration. In particular, the source distribution for the dipole oriented along the y-axis [Fig. 18(a)] is similar to the monopolar case [Fig. 13(b)], but the peak region extends more upstream, likely because the algorithm is able to additionally detect the source associated with the origin of the scattered field. For the solution linked to the dipole aligned with the x-axis [Fig. 18(b)], a nonnegligible contribution located at the physical-source position is found besides the low-amplitude spurious sources distributed along the x-dipole orientation.

In view of the above, the noise sources that characterize the sound maps for the baseline can be deemed as pure dipoles oriented along the y-axis, in line with the considerations made in Sec. II regarding the nature of the diffracted field. In contrast, the more complex directivity of the noise sources for the coated cylinder configuration suggests that the radiated sound is dominated by the y-dipole, but it also comprises additional source contributions that propagate in other directions. In other words, the acoustic field pictured here is consistent with a scenario where a lateral quadrupole in the wake radiates into the far field and is scattered by the body with a dipolar directivity. A 3D distribution of microphones should be designed so that the array can cover greater solid angles and detect higher-order multipoles with a higher level of accuracy.

REFERENCES

[1]V. Strouhal, "Ueber eine besondere Art der Tonerregung," Ann. Phys. Chem. **241**, 216–251 (1878).

[2]S. Rashidi, M. Hayatdavoodi, and J. Esfahani, "Vortex shedding suppression and wake control: A review," Ocean Eng. **126**, 57–80 (2016).

[3]T. Sueki, T. Takaishi, M. Ikeda, and N. Arai, "Application of porous material to reduce aerodynamic sound from bluff bodies," Fluid Dyn. Res. **42**, 015004 (2010).

[4]H. Naito and K. Fukagata, "Numerical simulation of flow around a circular cylinder having porous surface," Phys. Fluids **24**, 117102 (2012).

[5]H. Liu, J. Wei, and Z. Qu, "Prediction of aerodynamic noise reduction by using open-cell metal foam," J. Sound Vib. **331**, 1483–1497 (2012).

[6]J. Aguiar, H. Yao, and Y. Liu, "Passive flow/noise control of a cylinder using metal foam," in *the 23rd International Congress on Sound and Vibration* (International Institute of Acoustics and Vibration, 2016), p. 9.

[7]S. Showkat Ali, X. Liu, and M. Azarpeyvand, "Bluff body flow and noise control using porous media," in *22nd AIAA/CEAS Aeroacoustics Conference* (American Institute of Aeronautics and Astronautics, Lyon, France, 2016).

[8]T. Geyer and E. Sarradj, "Circular cylinders with soft porous cover for flow noise reduction," Exp. Fluids **57**, 30 (2016).

[9]T. Geyer, "Experimental evaluation of cylinder vortex shedding noise reduction using porous material," Exp. Fluids **61**, 153 (2020).

[10]E. Arcondoulis, Y. Liu, Z. Li, Y. Yang, and Y. Wang, "Structured porous material design for passive flow and noise control of cylinders in uniform flow," Materials **12**, 2905 (2019).

[11]E. Arcondoulis, Y. Liu, D. Ragni, F. Avallone, A. Rubio-Carpio, N. Sedaghatizadeh, Y. Yang, and Z. Li, "Internal shear layer and vortex shedding development of a structured porous coated cylinder using tomographic particle image velocimetry," J. Fluid Mech. **967**, A17 (2023).

[12]E. Arcondoulis, T. Geyer, and Y. Liu, "An investigation of wake flows produced by asymmetrically structured porous coated cylinders," Phys. Fluids **33**, 037124 (2021).

[13]E. Arcondoulis, T. Geyer, and Y. Liu, "An acoustic investigation of non-uniformly structured porous coated cylinders in uniform flow," J. Acoust. Soc. Am. **150**, 1231–1242 (2021).

[14]P. Bathla and J. Kennedy, "3D printed structured porous treatments for flow control around a circular cylinder," Fluids **5**, 136 (2020).

[15]R. Zamponi, F. Avallone, D. Ragni, C. Schram, and S. Van Der Zwaag, "Impact of quadrupolar-sound diffraction on flow-induced noise from porous cylinders" (2023).

[16]X. Gloerfelt, F. Pérot, C. Bailly, and D. Juvé, "Flow-induced cylinder noise formulated as a diffraction problem for low Mach numbers," J. Sound Vib. **287**, 129–151 (2005).

[17]M. Lighthill, "On sound generated aerodynamically I. General theory," Proc. R. Soc. London, Ser. A: Math. Phys. Sci. **211**, 564–587 (1952).

[18]N. Curle, "The influence of solid boundaries upon aerodynamic sound," Proc. R. Soc. London, Ser. A: Math. Phys. Sci. **231**, 505–514 (1955).

[19]M. Howe, *Acoustics of Fluid-Structure Interactions* (Cambridge University Press, Cambridge, 1998).

[20] S. A. L. Glegg and W. Devenport, *Aeroacoustics of Low Mach Number Flows: Fundamentals, Analysis, and Measurement* (Academic Press, London, 2017).

[21] R. Merino-Martínez, A. Rubio Carpio, L. Lima Pereira, S. van Herk, F. Avallone, D. Ragni, and M. Kotsonis, "Aeroacoustic design and characterization of the 3D-printed, open-jet, anechoic wind tunnel of Delft University of Technology," Appl. Acoust. **170**, 107504 (2020).

[22] R. Zamponi, F. Avallone, D. Ragni, and S. van der Zwaag, "On the aerodynamic-noise sources in a circular cylinder coated with porous materials," in *28th AIAA/CEAS Aeroacoustics 2022 Conference* (American Institute of Aeronautics and Astronautics, Southampton, UK, 2022).

[23] R. Porteous, D. Moreau, and C. Doolan, "A review of flow-induced noise from finite wall-mounted cylinders," J. Fluids Struct. **51**, 240–254 (2014).

[24] A. Rubio Carpio, R. Merino Martínez, F. Avallone, D. Ragni, M. Snellen, and S. van der Zwaag, "Experimental characterization of the turbulent boundary layer over a porous trailing edge for noise abatement," J. Sound Vib. **443**, 537–558 (2019).

[25] D. Ingham and I. Pop, *Transport Phenomena in Porous Media* (Elsevier, 1998).

[26] E. Baril, A. Mostafid, L. Lefebvre, and M. Medraj, "Experimental demonstration of entrance/exit effects on the permeability measurements of porous materials," Adv. Eng. Mater. **10**, 889–894 (2008).

[27] N. Dukhan and K. Patel, "Effect of sample's length on flow properties of open-cell metal foam and pressure-drop correlations," J. Porous Mater. **18**, 655–665 (2011).

[28] S. Sharma, T. F. Geyer, and E. J. Arcondoulis, "On the influence of porous coating thickness and permeability on passive flow and noise control of cylinders," J. Sound Vib. **549**, 117563 (2023).

[29] S. Luesutthiviboon, D. Ragni, F. Avallone, and M. Snellen, "An alternative permeable topology design space for trailing-edge noise attenuation," Int. J. Aeroacoust. **20**, 221–253 (2021).

[30] P. Welch, "The use of fast Fourier transform for the estimation of power spectra: A method based on time averaging over short, modified periodograms," IEEE Trans. Audio Electroacoust. **15**, 70–73 (1967).

[31] A. Brandt, *Noise and Vibration Analysis: Signal Analysis and Experimental Procedures* (John Wiley & Sons, 2011).

[32] T. Suzuki, "L1 generalized inverse beam-forming algorithm resolving coherent/incoherent, distributed and multipole sources," J. Sound Vib. **330**, 5835–5851 (2011).

[33] R. Merino-Martínez, P. Sijtsma, A. Rubio Carpio, R. Zamponi, S. Luesutthiviboon, A. Malgoezar, M. Snellen, C. Schram, and D. Simons, "Integration methods for distributed sound sources," Int. J. Aeroacoust. **18**, 444–469 (2019).

[34] R. Merino-Martínez, S. Luesutthiviboon, R. Zamponi, A. Rubio Carpio, D. Ragni, P. Sijtsma, M. Snellen, and C. Schram, "Assessment of the accuracy of microphone array methods for aeroacoustic measurements," J. Sound Vib. **470**, 115176 (2020).

[35] J. Hadamard, "Sur les problèmes aux dérivées partielles et leur signification physique," Princeton Univ. Bull. **13**, 49–52 (1902).

[36] R. Zamponi, N. V. de Wyer, and C. Schram, "An improved regularization of the generalized inverse beamforming applied to a benchmark database," in *Proceedings of the 7th Berlin Beamforming Conference* (GFaI, Gesellschaft zur Förderung angewandter Informatik e.V., Berlin, Berlin, Germany, 2018).

[37] C. Allen, W. Blake, R. Dougherty, D. Lynch, P. Soderman, and J. Underbrink, *Aeroacoustic Measurements* (Springer Berlin Heidelberg, Berlin, Heidelberg, 2002).

[38] P. Sijtsma, "Phased array beamforming applied to wind tunnel and fly-over tests," Technical Report No. 2010-36-0514 (National Aerospace Laboratory NLR, 2010).

[39] R. Zamponi, S. Satcunanathan, S. Moreau, D. Ragni, M. Meinke, W. Schröder, and C. Schram, "On the role of turbulence distortion on leading-edge noise reduction by means of porosity," J. Sound Vib. **485**, 115561 (2020).

[40] S. Tamaro, R. Zamponi, D. Ragni, C. Teruna, and C. Schram, "Experimental investigation of turbulent coherent structures interacting with a porous airfoil," Exp. Fluids **62**, 94 (2021).

[41] R. Zamponi, "Investigation of turbulence-surface interaction noise mechanisms and their reduction using porous materials," Ph.D. thesis (Delft University of Technology, 2021).

[42] J. Ffowcs Williams and L. Hall, "Aerodynamic sound generation by turbulent flow in the vicinity of a scattering half plane," J. Fluid Mech. **40**, 657 (1970).

[43] L. Milne-Thomson, *Theoretical Hydrodynamics* (Dover Publications, New York, 1996).

[44] T. Geyer, E. Sarradj, and C. Fritzsche, "Measurement of the noise generation at the trailing edge of porous airfoils," Exp. Fluids **48**, 291–308 (2010).

[45] A. Rubio Carpio, F. Avallone, D. Ragni, M. Snellen, and S. Van Der Zwaag, "Mechanisms of broadband noise generation on metal foam edges," Phys. Fluids **31**, 105110 (2019).